HOKKAIDO UNIVERSITY

Title	Pt/Ag Solid Solution Alloy Nanoparticles in Miscibility Gaps Synthesized by Cosputtering onto Liquid Polymers
Author(s)	Zhu, Mingbei; Nguyen, Mai Thanh; Chau, Yuen-Ting Rachel et al.
Citation	Langmuir, 37(19), 6096-6105 https://doi.org/10.1021/acs.langmuir.1c00916
Issue Date	2021-05-18
Doc URL	https://hdl.handle.net/2115/85105
Rights	This document is the Accepted Manuscript version of a Published Work that appeared in final form in Langmuir, copyright © American Chemical Society after peer review and technical editing by the publisher. To access the final edited and published work see https://pubs.acs.org/articlesonrequest/AOR-MDMCH4EPSNUDIQAN2KR8 .
Type	journal article
File Information	SubL-mingbei-NO review mark-4.pdf

Hokkaido University Collection of Scholarly and Academic Papers : HUSCAP

Pt/Ag Solid Solution Alloy Nanoparticles in Miscibility Gap Synthesized by Co-Sputtering onto Liquid Polymer

Mingbei Zhu,[1] Mai Thanh Nguyen,[1,] Yuen-ting Rachel Chau,[1] Lianlian Deng,[1] Tetsu Yonezawa[1,2,*]*

[1]Division of Materials Science and Engineering, Faculty of Engineering, Hokkaido University, Kita 13 Nishi 8, Kita-ku, Sapporo, Hokkaido 060-8628, Japan

[2]Institute of Business-Regional Collaboration, Hokkaido University, Kita 21 Nishi 11, Kita-ku, Sapporo, Hokkaido, 001-0021, Japan

[*]Email: mai_nt@eng.hokudai.ac.jp, tetsu@eng.hokudai.ac.jp

ABSTRACT

Pt/Ag solid solution alloy nanoparticles (NPs) with mean size below 3 nm were obtained with composition in miscibility gap by co-sputtering onto liquid polyethylene glycol (PEG, M. W. = 600). Adjusting the sputtering currents from 10 to 50 mA did not influence the particle sizes obviously but caused a substantial difference in the composition and distributions of Pt/Ag NPs. This is different from sputtered Pt/Au NPs where particle size is correlated with composition. For a pair of sputtering currents, the formed Pt/Ag alloy NPs have a range of compositions. The normal distribution with Pt of 60.2 ± 16.2 at.% is observed for Pt/Ag sample with nominal Pt content of 55.9 at. % whereas Pt rich (85.1 ± 14.0 at.% Pt) and Ag rich (19.8 ± 12.2 at.% Pt) Pt/Ag samples with nominal Pt content of 90.9 and 11.9 at.% contain more pure Pt and pure Ag NPs, respectively. Different from NPs obtained in PEG, the sputtered NPs on TEM grids had more uniform composition for a longer sputtering time along with a significant increase of particle sizes. This reveals that PEG hindered the combination of NPs and clusters, resulting in small particle sizes even for long time sputtering and broader composition distributions. Thus, the samples obtained in PEG have the compositions mainly determined by the random atom combination in the vacuum chamber and possibly in initial landing of atom/clusters on the PEG surface.

KEYWORDS. Pt/Ag, alloy nanoparticles, solid solution, sputtering onto liquid, liquid polymer, formation mechanism

Introduction

Pt nanoparticles (NPs) have been used as active catalysts for various reactions.[1-5] However, the high cost of scarce Pt metal impedes their practical applications.[6-11] To solve this problem, Pt has been made in alloy with cheaper metals, which can allow for attaining active catalysts at a lower cost.[6,12] For example, Pt/Ag alloy NPs show better catalytic activity and catalyst durability compared with pure Pt NPs.[13-15] This is because the alloying could modify the electronic structure of Pt and generate lattice distortion for improving the electrocatalytic performances.[13-15] Pt and Ag form some intermetallic compounds and there are big miscibility gaps in the bulk phase diagram.[16] The formation of alloy becomes more feasible in small NPs wherein the enhanced metal diffusion and mixing and higher thermodynamic stability can be achieved.[17,18] Pt/Ag alloy NPs with various sizes and compositions have been reported by a reduction at elevated temperature or by electrochemistry.[6,12,19-22] For example, P. Song et al. synthesized Pt/Ag alloy NPs of about 54 at. % Pt with variable sizes from 7.5 to 15 nm for catalytic electrooxidation of liquid fuels.[6] They demonstrated the best electrocatalytic activities for Pt/Ag NPs of the smallest size.[6] Z. Li et al. prepared Pt/Ag alloy NPs with 50 and 66 at. % of Pt and an average size of ~2.5 nm supported by graphene conductive networks for advanced oxygen reduction reaction electrocatalysts.[12] However, at lower content of Pt, they obtained segregated Ag and Pt/Ag alloys.[12] Therefore, synthesis of alloy Pt/Ag NPs of controlled size and composition is demanded.

Sputtering is a conventional physical technique for the fabrication of thin films

or creation of NPs directly on solid substrates from the bulk target in vacuum and dry conditions.[23,24] Non- or low volatile liquids as the substrates,[25-35] e.g., silicone oils,[25] ionic liquids,[26,27,30,31] and liquid polymers,[28,32-35] have been used for obtaining NPs dispersed in liquids for a long time continuous sputtering. Compared with the traditional chemical reduction method, co-sputtering can simultaneously produce metal atoms and clusters of two or more metals for making alloy NPs at room temperature regardless of the difference in redox potentials of metals and without using toxic reductants.[30-35] Moreover, it is capable of varying the properties of NPs by varying the size, composition, composition distribution, and structures of NPs via adjusting the sputtering parameters such as the currents applied to the metal targets.[30-35] Co-sputtering onto liquid allows obtaining solid solution alloys of metal pairs that have miscibility gaps and/or form intermetallic compounds in phase diagram such as Au/Pd, Pt/Au, Au/Cu, and Cu/Pd.[30-35] However, so far there has been no report on co-sputtering onto liquid at room temperature of Pt/Ag NPs below 3 nm, their fine structure, and whether solid solution alloy can be attained, especially for the composition in the miscibility gap. Further, the correlation of particle size and composition varied with the metal pairs, that is, the size-composition relation is not obvious in co-sputtered Au/Cu and Cu/Pd whereas highly correlated in Pt/Au NPs.[33-35] This relation has not been addressed for co-sputtered Pt/Ag NPs. Therefore, we chose to synthesize Pt/Ag alloy NPs at room temperature by co-sputtering onto liquid polyethylene glycol (PEG), a biocompatible and cheap liquid, and investigate the fine structure and composition of the resulting NPs in the present study. The obtained Pt/Ag NPs were analyzed by UV-

Vis, TEM, HR-TEM, STEM, EDS, and XRD. The results proved that Pt/Ag NPs have a solid solution structure. We found that the sputtering currents applied to the targets had little effect on the average sizes, but they could vary the particle compositions and had impacts on the composition distributions of the samples. Comparing the compositions and particle sizes of the NPs sputtered onto PEG and on TEM grids, we address the impact of the substrate in the formation and growth of particles. We found that in the presence of PEG, the composition could be determined by the random combination of metal atoms/clusters in the sputtering chamber with less change after the growth of NPs in PEG.

Experimental section

Materials

PEG (M. W. = 600, Junsei, Japan), Pt target (99.99% in purity, 50 mm in diameter, Tanaka Precious Metals, Japan), Ag target (99.99% in purity, 50 mm in diameter, Tanaka), and TEM grids (Nisshin EM, Japan) were used.

Synthesis of PtAg alloy nanoparticles

The co-sputtering method has been reported elsewhere.[32-35] In the present study, PEG was stirred (650 rpm) under vacuum in the flask in an oil bath at 90 °C for at least 2 h to remove water and gases. Then 10 mL of PEG was added into a Petri dish with a diameter of 60 mm which was located horizontally in the center of a magnetron sputtering vacuum chamber, a stirrer was put under the PEG surface. PEG was under stirring at 80 rpm during sputtering. Pt and Ag targets were used in this co-sputtering

technique, and elemental ratios of the formed Pt/Ag NPs were controlled by adjusting the sputtering current applied to each sputtering target (10~50 mA). PEG, carbon-coated Cu transmission electron microscopy (TEM) grids, and glass slides were used as the substrate for sputtering experiments. When a TEM grid was used as the substrate, it was placed at the center of the Petri dish. The center of the surface of PEG and TEM grids was located at a distance of 110 mm from the two metal targets. Similarly, glass slides were located at the center position of the Petri dish. After several times of vacuum and gas exchanging with inert Ar to remove O_2, the pressure of the vacuum chamber was kept constant at 2 Pa. Cooling ethanol of 0 °C was used for cooling the metal targets during sputtering. In all the sputtering experiments, before collect NPs, Pt and Ag targets were sputtered for 10 min to clean the target surface. During this period removable shutters located in front of metal targets and on top of the liquid polymer were used to prevent the contamination from falling onto the liquid. Sputtering onto PEG was conducted for 30 min whereas sputtering onto the TEM grids was conducted for 1 s to 2 min with the TEM grids. The applied sputtering current was varied from 10 to 50 mA for two metal targets and the total mass of Pt/Ag in PEG was 0.85 – 2.24 mg (Table 1). The sputtering system was equipped with a thermocouple and a temperature-controlled system to keep the substrate temperature at 30 °C.

Characterization

UV-Vis spectra were collected immediately after sputtering deposition by JASCO V-630 spectrophotometer using a quartz cuvette with an optical path of 1 mm. All spectra were baseline corrected using an empty quartz cuvette. The size and shape of the NPs

were obtained from TEM (JEOL JEM-2000FX, 200 kV). High-resolution TEM (HR-TEM) and scanning TEM (STEM) images were obtained using a JEOL JEM-ARM200F operating at 200 kV. Samples for TEM, HR-TEM, and STEM analysis were prepared by dipping a grid into PEG dispersion for about 10 s, then immediately dipping into ethanol for at least 20 min to remove the excess amount of PEG, and finally drying in the air at room temperature for a few minutes. Size and size distributions were collected from TEM, HR-TEM, and STEM images by measuring approximately 150 particles in at least three different regions of the grid using ImageJ software. The structure of NPs was evaluated using high-angle annular dark-field (HAADF)-STEM and X-ray diffraction (XRD, Rigaku Mini Flex II, Cu Kα radiation, $\lambda = 1.5418$ Å, scanning speed of 0.5 °/min). XRD samples were prepared by addition of excess acetone into PEG-NPs dispersion then centrifuged multiple times at 10000 rpm for 10 min each time for isolating Pt/Ag NPs from PEG. The purified Pt/Ag sample precipitate in acetone after a day. The X-ray intensities for all samples were plotted as a function of 2 theta and were normalized. Elemental mapping using energy-dispersive X-ray spectroscopy (EDX) coupled with STEM (JEOL JEM-ARM200F) was carried out to verify the existence of Pt/Ag alloy NPs and their composition. An X-ray photoelectron spectroscope (XPS, JEOL, JPS-9200, Al Kα source) was used to collect XPS spectra of NPs sputtered onto PEG for 30 min and on Si wafer for 10 s. Graphite was added to PEG dispersion to collect NPs, then the dispersion was centrifuged and washed with acetone several times to separate and purify the Pt/Ag NPs from PEG. The C 1s of graphite at 284.2 eV was used for charge correction. For samples sputtered on Si wafer,

Si 2p at 99.2 eV was used for charge correction. Energy pass of 20 eV and 10 eV was used for collecting XPS spectra of samples in PEG and on Si wafer. A higher energy pass was used for the sample sputtered onto PEG because at low energy pass the intensity is insufficient to be distinguished from the background.

Results and discussion

To distinguish the samples synthesized with different currents applied to the Pt and Ag targets, the samples are labeled with the metals and corresponding applied sputtering currents. For example, the sample Pt50Ag50 represents a sample synthesized by co-sputtering with the currents of 50 mA for Pt and Ag targets.

TEM images and UV-Vis spectra of Pt/Ag NPs

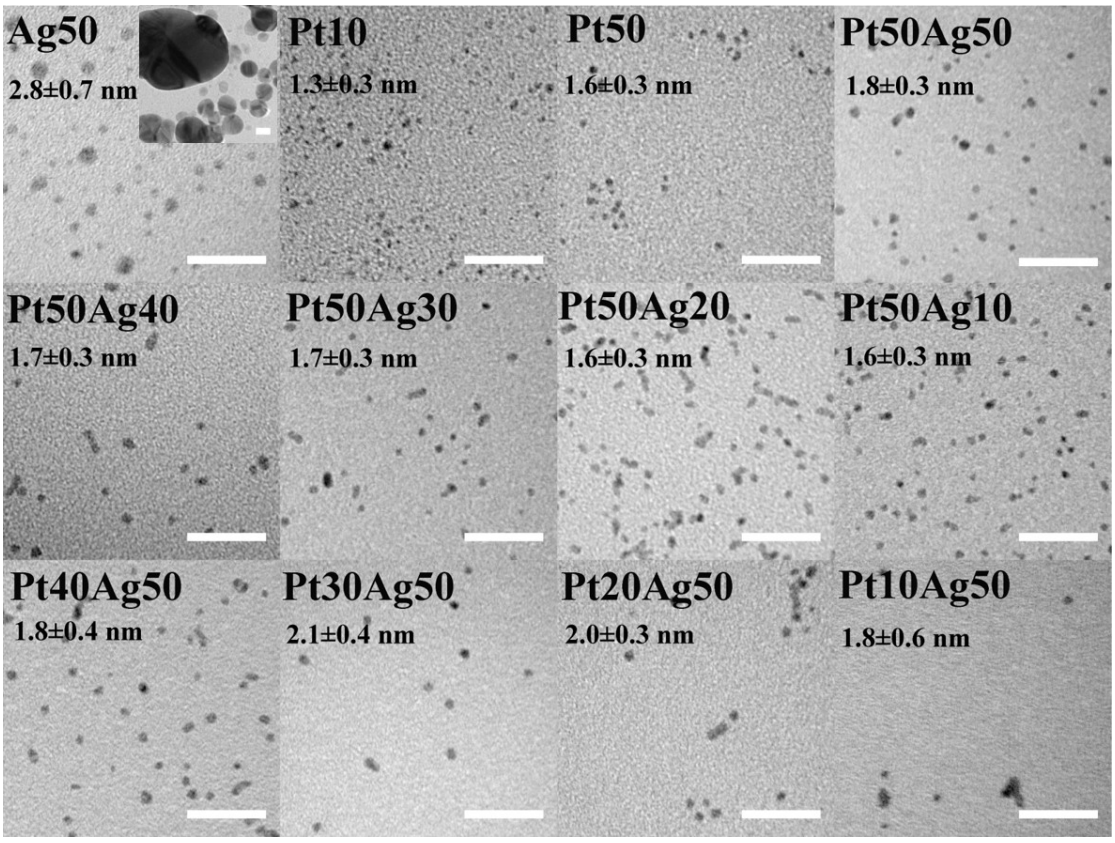

Figure 1. TEM images of Ag, Pt, and co-sputtered Pt/Ag samples. The scale bar in white is 20 nm. The average particle sizes are shown in the images.

Figure 1 shows the bright-field TEM images of Pt NPs, Ag NPs, and the co-sputtered Pt/Ag alloy NPs. The size distributions of samples Pt50Ag(10~50) and Pt(10~50)Ag50

are shown in Figures S1 and S2, respectively. The results were obtained by measuring the diameters of nearly spherical NPs. Ag50 contained big Ag NPs (inset of Figure 1) and small Ag NPs of 2.8 ± 0.7 nm. Pt10 and Pt50 had average particle diameters of 1.3 ± 0.3, 1.6 ± 0.3 nm, respectively. The average sizes of Pt50Ag(10~50) samples increased from 1.6 ± 0.3 to 1.8 ± 0.3 nm as the sputtering current of Ag increased from 10 to 50 mA and that of Pt constant at 50 mA. The Pt(10~50)Ag50 samples with an average size of 1.8 ± 0.3, 1.8 ± 0.4, and 1.8 ± 0.6 nm were obtained when the sputtering current for Pt is 10, 40, and 50 mA, respectively. The broader size distribution was observed when using a low sputtering current for Pt, i.e., 10 mA (Figure S2), and some big particles were observed in the sample. The mean size of Ag/Pt NPs slightly increased to 2.0 ± 0.3 and 2.1 ± 0.4 nm for Pt20Ag50 and Pt30Ag50 samples, respectively. This result indicated that the currents applied to the metal targets in the range of 10-50 mA did not have a significant impact on the particle sizes of the samples and a sample of a higher content of Ag generally has a slightly bigger particle size. Overall, the particle sizes of Pt/Ag alloy NPs are smaller than that of pure Ag NPs. This is similar to the results observed in co-sputtered Pt/Au and Au/Cu NPs into PEG in which the alloy NPs have a size in between that of the monometallic NPs.[33,34] However, different from Pt/Au alloy NPs with a strong correlation of size and composition (regulated by sputtering current),[34] such correlation is not obvious in Pt/Ag NPs. This is similar to co-sputtered Au/Cu NPs in PEG.[33]

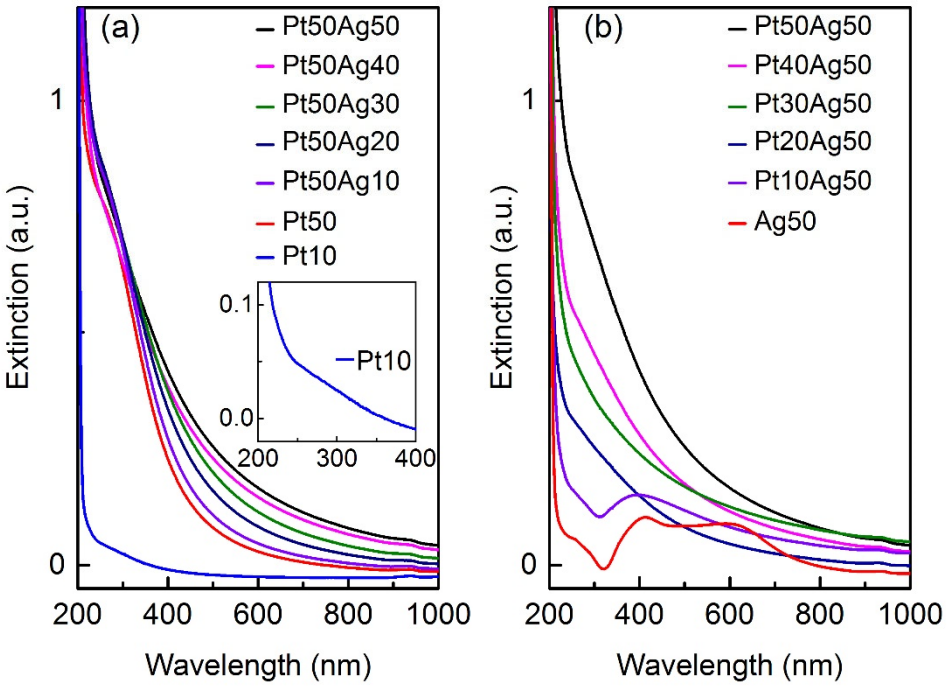

Figure 2. UV-Vis spectra of the Pt/Ag alloy NPs synthesized under different sputtering currents: (a) 50 mA for Pt and 0~50 mA for Ag target; (b) 0~50 mA for Pt and 50 mA for Ag target. UV-Vis spectrum of Pt NPs sputtered at 10 mA is shown in Figure 2a and its inset shows the magnified spectrum with the horizontal axis from 200 to 400 nm.

After sputtering, the samples (Figure S3) were collected and analyzed with UV-Vis. Figure 2a shows the UV-Vis spectra of the samples Pt50Ag50, Pt50Ag40, Pt50Ag30, Pt50Ag20, Pt50Ag10, and Pt50. There was an absorption shoulder at around 280 nm in these samples, which indicated the presence of Pt in the PEG dispersion. The intensity of this shoulder for Pt/Ag samples sputtered using the applied current to Pt target of 50 mA and Pt50 sample did not vary significantly because it was related to the concentration of Pt. It could be seen that sample Pt10 (inset of Figure 2a) had a similar

absorption shoulder with lower intensity compared with sample Pt50. This is because the lower sputtering current for Pt target produced the more dilute Pt/PEG dispersion. There was no localized surface plasmon resonance (LSPR) of pure Ag NPs in all of these co-sputtering samples Pt50Ag(10~50). Further, the absorption intensity above 350 nm of these samples increased with the increase of the applied current for Ag thereby increase of Ag content in the Pt/Ag NPs. These results indicated a possible alloy formation between Pt and Ag.

For the samples Pt(0~50)Ag50, the UV-Vis spectra (Figure 2b) also showed the broad absorption shoulder around 280 nm associated with the presence of Pt in the samples. Overall in low wavelength region (below 400 nm) the absorption intensity increased as the applied current of Pt increased. This demonstrated the correlation between the concentration of Pt and the intensity of the absorption shoulder at 280 nm. Further, the spectra of Ag50 and Pt10Ag50 showed an LSPR peak at around 400 nm, which is the typical characteristic of Ag NPs. And there is also an absorption peak at around 600 nm in the spectrum of Ag50 owing to the existence of some aggregation and/or agglomeration in the sample. This result is consistent with TEM results and suggests that PEG stabilizes Pt better than Ag and Ag-rich Pt/Ag NPs. This absorbance decreased with increasing the applied currents to Pt from 0 to 20 mA, indicating that alloying Pt and Ag suppressed the formation of pure Ag NPs and the agglomeration. Further increasing the sputtering currents applied to Pt from 20 to 50 mA, the absorption peak at 400 nm belongs to pure Ag NPs disappeared. Thus, the UV-Vis results obtained by varying the sputtering currents of Ag and Pt suggested the formation of Pt/Ag alloys

in the co-sputtered samples. To confirm the formation of solid solution alloy in Pt/Ag NPs, we further analyzed the structure and composition of samples with XRD, HAADF images, STEM-EDX mappings, and XPS.

Crystal structures of Pt/Ag NPs

To analyze the structure of the co-sputtered Pt/Ag alloy NPs, the NPs synthesized by double head sputtering onto PEG were separated from PEG and their XRD patterns were collected. The XRD results are shown in Figure 3a. The diffraction peaks of samples Pt50Ag50 and Pt10Ag50 were located between the peaks of Pt and Ag reference. The (111) peak position of Pt50Ag50 (2θ = 39.4°) was closer to that of reference Pt (2θ = 39.8°) and farther to that of reference Ag (2θ = 38.1°) when compared to that of Pt10Ag50 (2θ = 38.1°). This indicated sample Pt50Ag50 had a higher composition of Pt compared with the sample Pt10Ag50. Further, the (111) peak of Pt50Ag50 was symmetric whereas that of Pt10Ag50 was somehow as-symmetric with more broadening to the right. This indicates that in the sample Pt10Ag50, Pt/Ag grains with the sharp feature may contain slightly more Ag compared to the sample with smaller grain sizes, which we will confirm later with STEM-EDS mapping (Figure S4). The average grain size estimated from line broadening of (111) XRD peak using Scherrer equation resulted in a size of 4 and 15 nm for Pt50Ag50 and Pt50Ag10 NPs, respectively. The large grain size found in Pt50Ag10 is understandable as larger crystals even in a smaller population can contribute more significant signals compared with the small ones. We observed that Pt10Ag50 and Pt50Ag50 NPs could be separated from

PEG by centrifugation. However, this method was not sufficient to obtain the precipitate of Pt50Ag10 NPs. This is consistent with the TEM results that this sample had the smallest size (1.6 ± 0.3 nm) among all co-sputtered Pt/Ag samples (Figure 1). Besides, Pt50Ag10 sample with the highest content of Pt in Pt/Ag alloy NPs and small sizes can be stable enough in PEG, which was similar to our previous observation for sputtered Pt and Pt-rich Pt/Au NPs.[34] In an attempt to collect the Pt50Ag10 NPs, we added some fume SiO_2 into the PEG dispersion containing Pt50Ag10 NPs first to adsorb Pt/Ag NPs before using the centrifugation to separate NPs/SiO_2 from PEG. Unfortunately, there was no peak detectable in Pt50Ag10. Judging from the results, we think that the amount of Pt50Ag10 NPs separated from PEG was too small and/or their crystallinity was not good.

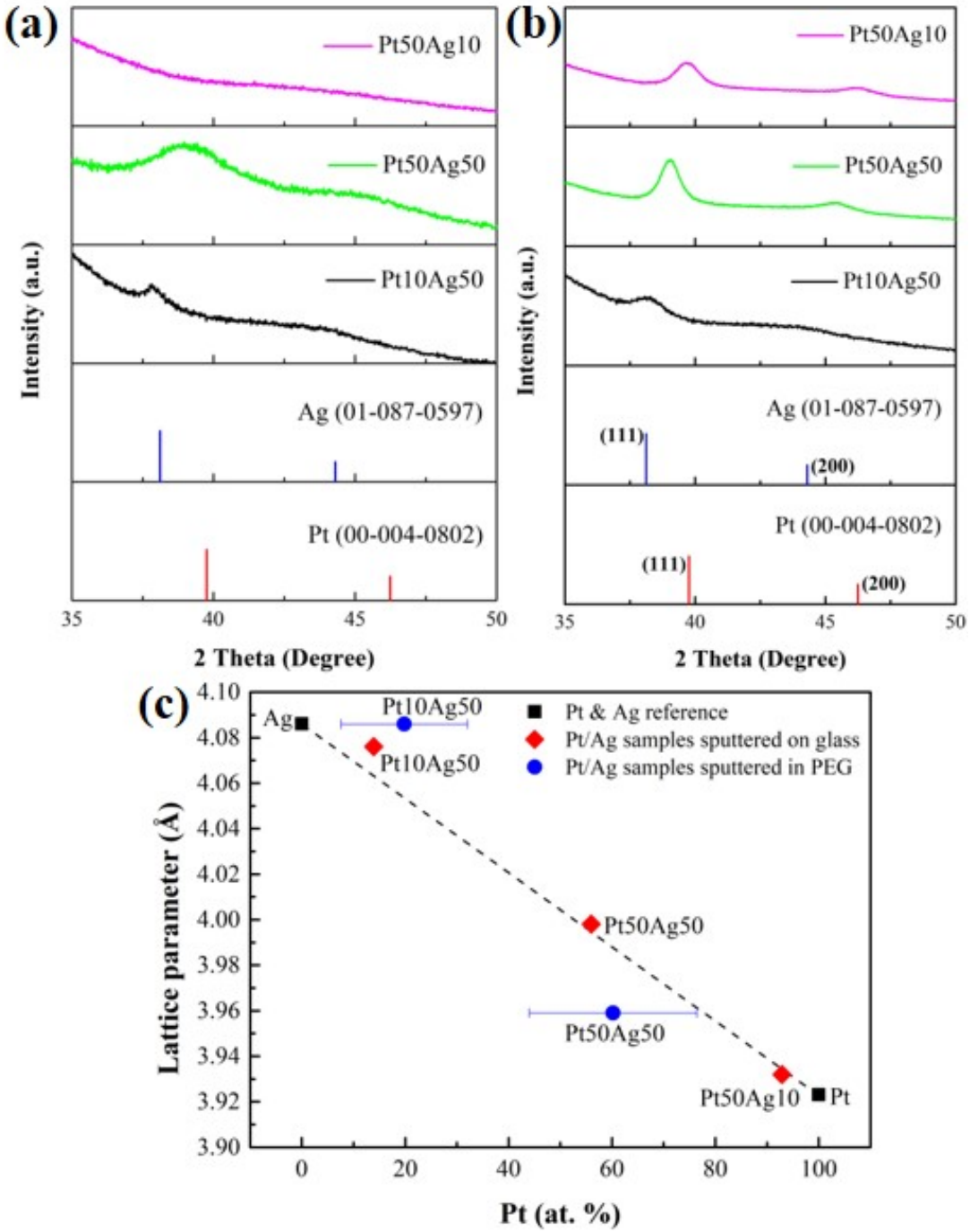

Figure 3. (a) XRD patterns of Pt50Ag10, Pt50Ag50, and Pt10Ag50 deposited in PEG. (b) XRD patterns of Pt50Ag10, Pt50Ag50, and Pt10Ag50 sputtered on glass for 2-5 min. Stick patterns are characteristic diffraction peaks from (111) and (200) planes of reference Pt (JCPDS No. 00-004-0802) and Ag (JCPDS No. 01-087-0597). (c) Relation between lattice parameter estimated from XRD peak positions of (111) planes and

atomic compositions of Pt in Pt/Ag. The compositions of Pt/Ag in PEG and on glass were measured with STEM-EDS and mass measurement (Table 1), respectively. Error bars are standard devidations of the compositions measured by STEM-EDS for Pt/Ag obtained in PEG. The lattice parameters of Ag and Pt from the above XRD reference in Figures 3a and b were used. The black, dashed line connecting Ag and Pt shows the ideal relation for Pt/Ag alloys which follows Vegard's law.

Consequently, the experiments of co-sputtering of Pt and Ag directly on glass slides for different sputtering currents and times were carried out to get more insight (Figures 3b and S5). Figure 3b shows that the (111) peak positions of Pt10Ag50, Pt50Ag50, and Pt50Ag10 samples that sputtered on glass slides for 5 min were 38.21, 39.01, and 39.67°, respectively. The peaks were between (111) peaks of the reference Ag and Pt. Further, there was a clear trend in the peak positions among 3 samples, that is the (111) peak shifts in the direction from Ag towards Pt with increasing Pt content by varying the sputtering currents applied to Pt and Ag targets. The lattice parameters obtained from the (111) XRD peak positions of the samples sputtered on glass showed a linear relationship with the sample composition (Figure 3c). This followed Vegard's law[36] and indicated the formation of solid solution alloys of Pt/Ag on glass. The results for Pt/Ag NPs sputtered onto PEG show certain deviations from the ideal relation. This indicated that (i) some sputtered NPs with different compositions may remain in PEG and not able to be separated for XRD analysis, (ii) formation of the crystal structure is incomplete, and/or (iii) the measured composition distributed in a large range.

We also observed that varying the sputtering times onto glass substrate from 2 min to 30 min did not change the peak position for sample Ag50Pt50 (Figure S5). However, the smallest time of sputtering for the Bragg diffraction peaks appearing in the XRD pattern was different depending on the samples. For example, when the sputtering time on glass was 2 min, fairly weak (111) diffraction peak of Pt50Ag10 (Figure S6) and clear (111) peak of Pt50Ag50 sample (Figure 3b) were detected whereas no peak was observed for Pt10Ag50 (Figure S6). It required 5 min sputtering to observe weak signals of typical diffraction peak in the sample Pt10Ag50 (Figure 3b). The possible reason could relate to the amount and crystallinity of Pt/Ag NPs. Higher sputtering currents and time resulted in more metal atoms in the sputtering chamber, thus leading to a higher amount of NPs and possibly the formation of larger grain size, for which the XRD signals of Pt/Ag crystals were more significant. On this basis, for the same sputtering time, Pt50Ag50 had the largest amount of atoms and thus, it had the most profound peaks among 3 samples. The sputtering rate of Pt is slightly higher than that of Ag (Table S1) and it took a shorter time of sputtering for Pt50Ag10 compared with Pt10Ag50 for the clear appearance of XRD peaks.

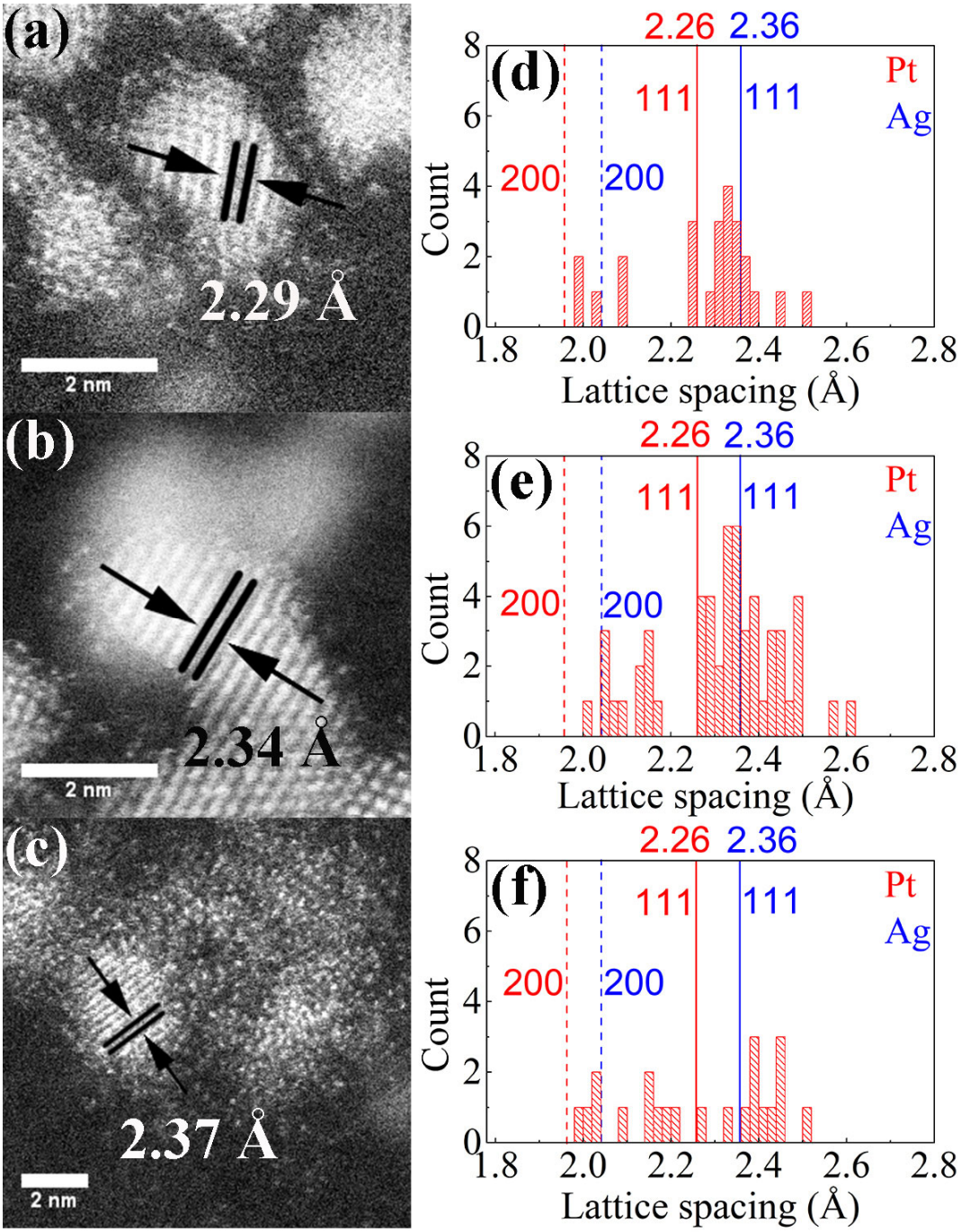

Figure 4. HAADF images of (a) Pt50Ag10, (b) Pt50Ag50 and (c) Pt10Ag50 samples obtained in PEG. The lattice spacings are shown in the pictures. Lattice parameter distributions of (d) Pt50Ag10, (e) Pt50Ag50 and (f) Pt10Ag50. Solid and dashed lines represent the lattice parameters of (111) and (200) planes, respectively, of Pt (in red) and Ag (in blue). The numbers of the particles measured are 24, 55, and 23 for samples Pt50Ag10, Pt50Ag50, and Pt10Ag50, respectively.

Figures 4a-4c present the STEM-HAADF images of co-sputtered Pt/Ag alloy NPs with clear lattice fringes. The lattice spacings of samples Pt50Ag10 Pt50Ag50, and Pt10Ag50 were measured to be 2.29 Å, 2.34 Å, and 2.37 Å, respectively. The lattice spacing of (111) plane in reference Pt (JCPDS No. 00-004-0802) and Ag (JCPDS No. 01-087-0597) are 2.26 Å and 2.36 Å, respectively. The lattice spacing of Pt10Ag50 was slightly larger than that of Pt50Ag50 and Pt50Ag10, which was caused by a larger content of Ag in Pt10Ag50, and the lattice spacing of reference Ag is bigger than that of Pt. It was noticed that the lattice spacing of Pt10Ag50 (2.37 Å) was a little bit larger than that of reference Ag (2.36 Å), this could be caused by the small sizes and thus, swelling of the crystal structure. The statistical analysis of the lattice spacings using HAADF images (Figures 4d-4f) of three samples, Pt50Ag10, Pt50Ag50 and Pt10Ag50, consistently showed the lattice spacing distributions and the peaks of this distribution varied with the sample compositions wherein sample with more Pt had the peak of (111) lattice spacings closer to pure Pt. Further, the higher composition of Ag in Pt/Ag samples likely caused an increase in the fraction of NPs with larger lattice spacings compared with that of (111) plane in pure Ag as observed in HAADF images. The exact reason is not clear, but, this can associate with the expansion in crystal structures of Ag rich Pt/Ag NPs under STEM observation.

Discussion in solid solution and intermetallic compound structure of Pt/Ag NPs. Three intermetallic compounds[16] with Pt at. % of 45 ($Ag_{55}Pt_{45}$), 50 (AgPt), and 75 ($AgPt_3$) and only intermetallic compound[37] of $Ag_{15}Pt_{17}$ (53 at. % Pt) are shown in the phase diagram given by Karakaya et al[16] and Okamoto,[37] respectively. These

intermetallic compounds are at 400 °C or more. Experimental data for the annealed samples at high temperature 750 °C for 80 days by Hart et al.[38] supports the existence of the ordered $L1_1$ structure at about 50 at. % Pt. The calculated structures of bimetallic Pt-Ag (including un-stable phases) suggest AgPt trigonal, AgPt hexagonal, $AgPt_3$ cubic, Ag_3Pt cubic, and $AgPt_4$ trigonal structure.[39] Two un-stable phases (cubic $AgPt_3$ and Ag_3Pt) can decompose as: $AgPt_3 \leftrightarrow AgPt_4 + AgPt$ and $Ag_3Pt \leftrightarrow Ag + AgPt$.

Our XRD results indicate the co-sputtered Ag/Pt NPs have a cubic structure, thus, we exclude the existence of trigonal, hexagonal intermetallic compounds. $Pt_{50}Ag_{50}$ NPs have a composition of 60.2 ± 16.2 at % Pt (Table 1). The composition range locates in the miscibility gap in the above phase diagrams and possibly contains cubic $AgPt_3$ (75 at. % Pt) and $L1_1$ AgPt (50 at. % Pt) compounds. However, no obvious peak separation or as-symmetry in the XRD pattern of Ag50Pt50 (Figure 3), suggesting that the XRD peaks do not comprise two intermetallic compounds.

If $L1_1$ ordered AgPt NPs (50 at. % Pt) are the majority of Ag50Pt50 sample, 13 % of NPs can have the right orientation with the zone axis parallel to (111) plane to be observed with the ordered $L1_1$ structure (assuming the random orientation of NPs on the grid for STEM).[40] We analyzed the STEM-HAADF images of Pt50Ag50 NPs (>200 particles) with many NPs align in the zone axis along (111) planes. However, the arrangement of the ordered $L1_1$ structure with alternating dark and brighter contrast for Ag and Pt (111) was not found. The uniform and random contrast of the atom columns belong to (111) planes in NPs was observed (an example is shown in Figure 5). This

indicates the disordered solid solution structure with mixed Pt and Ag in each atom column of (111) planes.

Besides, annealing at high temperatures is often necessary to form the intermetallic compounds (ordered structures). Torimoto reported the conversion of the sputtered fcc-solid solution alloy AuCu NPs to the ordered $L1_0$ intermetallic compound by annealing (> 150 °C).[41] Peng et al. reported that chemically synthesized Pt/Ag NPs at 260 °C for 1 h are solid solution alloy for Pt of 20-80 at. %.[42] This suggests that 260 °C and 1 h reaction is insufficient to form the intermetallics. Under simultaneously atomic condensation of Ag and Pt sources in an ultra-high vacuum chamber, Pirat et al. observed fcc disordered Ag/Pt alloy NPs (50 at. % Pt).[40] After annealing at 400 °C, they observed the ordered $L1_1$ Ag/Pt intermetallic NPs.[40] However, no annealing was conducted for our samples and this fact must be taken into account when considering the crystal structure of Pt/Ag. Hence, based on the results of XRD, the relation of lattice-parameter and composition among samples of different Pt at %, d-spacings, and intensity profile we assign the obtained structure in our co-sputtered Ag/Pt NPs as solid solution alloy. Though we could not prove that there is completely no intermetallic compound, we are confident that the disordered solid solution alloy NPs are the majority under our synthesis conditions.

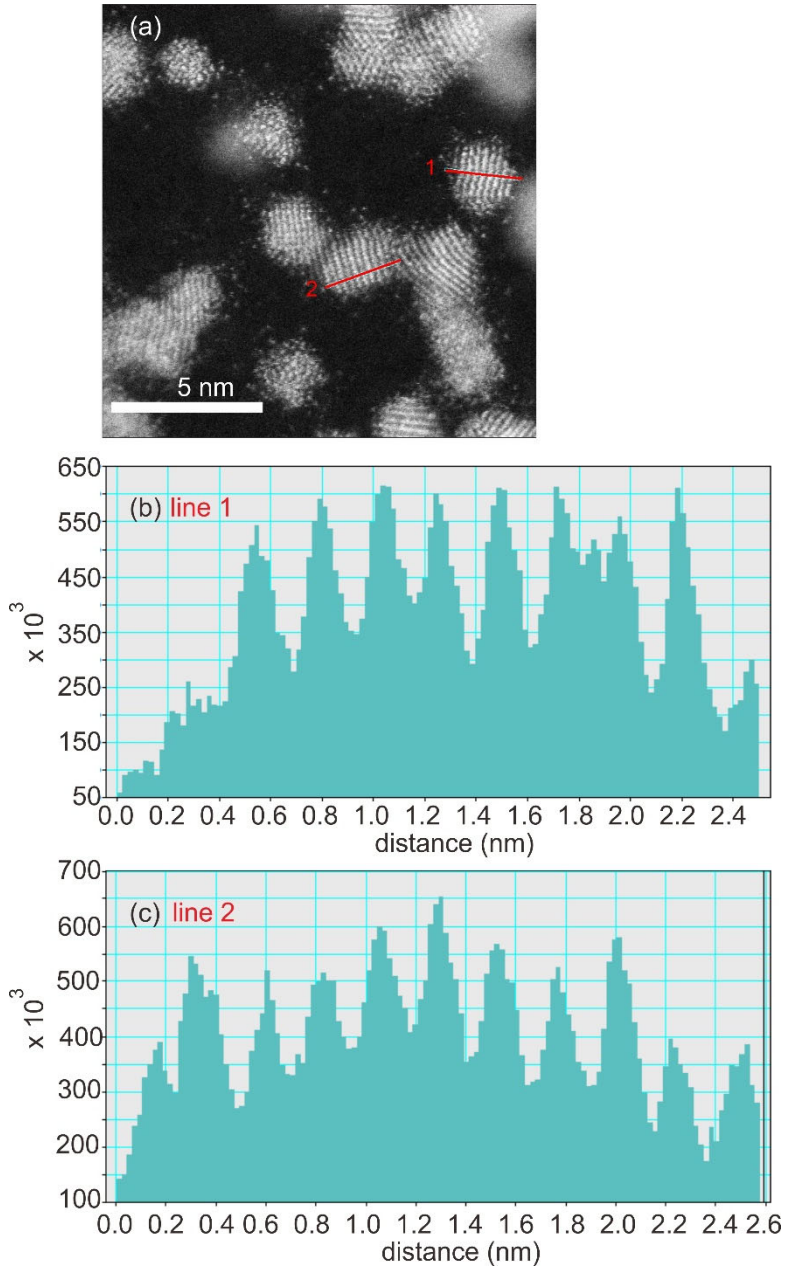

Figure 5. (a) HAADF image of Pt50Ag50 NPs sputtered onto PEG with particles showing (111) planes parallel to the zone axis. (b,c) Intensity profiles for atom columns of (111) planes in the red lines 1 and 2 in (a), respectively. (b) Uniform and (c) random intensity contrast show the mixed Pt and Ag in each atom column of the (111) planes.

XPS analysis of Pt/Ag NPs

Figure 6 shows XPS narrow scans of Pt 4f and Ag 3d of Pt50Pt50 sputtered onto PEG. Two components, namely, Pt-1 at 71.29 ($4f_{7/2}$), 74.59 eV ($4f_{5/2}$) and Pt-2 at 73.01 ($4f_{7/2}$) and 76.31 eV ($4f_{5/2}$) can be used to fit Pt 4f spectrum. The spin-orbit splitting of both components (3.3 eV) is the same as the reference for Pt.[43] However, the binding energy of Pt 4f of Pt-1 is close to whereas that of Pt-2 is 2.2 eV larger than the reference value (70.9 eV for Pt $4f_{7/2}$).[43] Ag 3d spectrum can be deconvoluted using 4 components, that is, Ag-1 at 367.36 ($3df_{5/2}$) and 373.35 eV ($3df_{3/2}$), Ag-2 at 368.27 ($3df_{5/2}$) and 373.97 eV ($3df_{3/2}$), and 2 plasmon loss feature peak at 371.41 and 372.25 eV. The spin orbit-splitting of Ag-1 and Ag-2 component in Ag 3d spectrum is of 5.97 and 5.70 eV, respectively, which is lower than the reference value for Ag metal (6 eV).[43] The shoulder around 370 eV in Ag 3d is not completely fitted. Fitting Ag $3d_{5/2}$ and $3d_{3/2}$ with two curves still leaves a part of the shoulder unfitted and results in $3d_{5/2}$ and $3d_{3/2}$ with different FWHM (Figure S7). Possibly, a non-uniform charging effect occurred or a higher signal to noise ratio and higher intensity is required to distinguish the signal from noise. Ag-2 component has binding energy similar to metallic Ag whereas Ag-1 is closed to Ag oxide (note that binding energy of Ag^0 is higher than Ag oxide).[43] From the Ag 3d and Pt 4f narrow scans, the sample can contain Pt/Ag metal (Pt-1 and Ag-2) and partially oxidized Pt-Ag (Pt-2 and Ag-1). However, we cannot exclude the possibility of the size effect in the energy shift of Pt-2 and Ag-1.

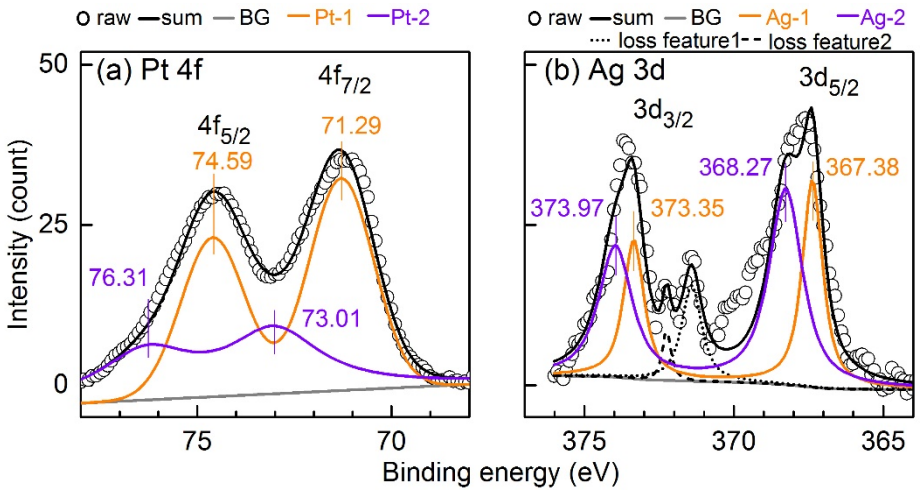

Figure 6. XPS spectra of Pt50Ag50 sputtered onto PEG for 30 min: (a) Pt 4f, (b) Ag 3d.

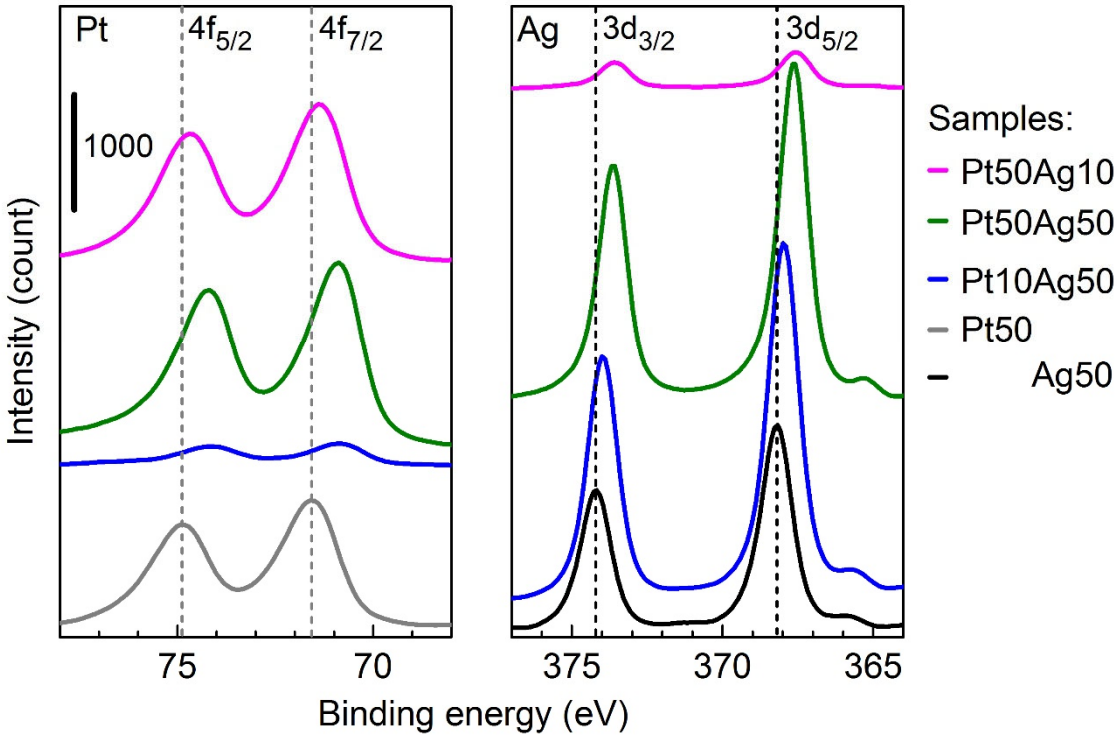

Figure 7. Narrow scan XPS spectra of Pt 4f and Ag 3d of the Pt50Ag10, Pt50Ag50, Pt10Ag50, Pt50, and Ag50 NPs sputtered on silicon wafers for 10 s. The dashed lines mark the peaks for the samples of Pt50 and Ag50 NPs.

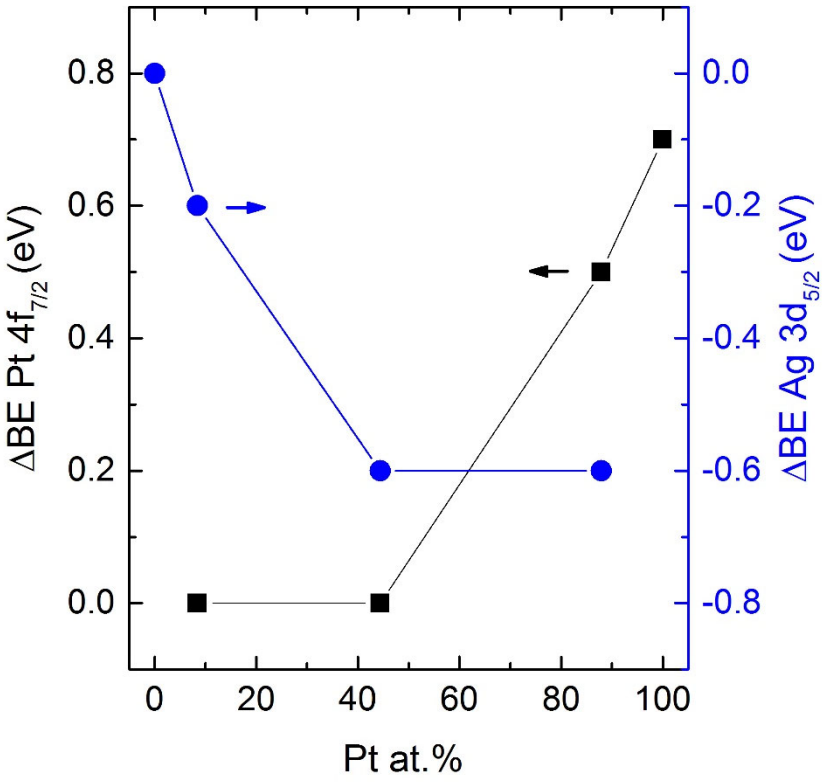

Figure 8. The correlation of the binding energy shift of Pt $4f_{7/2}$ and Ag $3d_{5/2}$ peaks and Pt atomic composition in Pt/Ag, Pt, and Ag NPs sputtered on Si for 10 s. The shift was obtained by subtracting the binding energy of Pt $4f_{7/2}$ and Ag $3d_{5/2}$ of NPs to the reference value of metallic Pt $4f_{7/2}$ (70.9 eV) and Ag $3d_{5/2}$ (368.2 eV), respectively. The composition was estimated using XPS analysis.

It is difficult to judge the alloying formation for NPs in PEG with confidence based on XPS. This is because the intensity is low (count < 50), high pass energy of 20 eV was required to increase the intensity (this lowers the spectrum resolution), the effect of Ar etching to remove PEG on the particle surface (e.g., oxidation), and possible

interference of the non-uniform charging effect after Ar etching (Figures 6 and S7). Thus, we also collected XPS spectra for Pt/Ag, Pt, and Ag NPs sputtered on Si wafer for 10 s with high energy resolution (pass energy of 10 eV) and sufficient intensity (more than 40 times higher than the samples obtained in PEG) as shown in Figure 7. 10 s sputtering allows to obtain separated NPs with size between 1.6 ± 0.3 (5 s sputtering) and 2.6 ± 0.3 nm (20 s sputtering) (Figure S18). This size range covers the size of NPs obtained in PEG. The spin-orbit splittings of Pt 4f and Ag 3d are the same as the reference for Pt and Ag, respectively. The binding energies of Pt 4f and Ag 3d peaks are given in Table S2. Figure 8 shows that for an increase of Pt at. % in NPs, the binding energy shift of Pt $4f_{7/2}$ is more positive compared with the bulk reference Pt whereas the shift of Ag $4d_{5/2}$ is more negative compared with the bulk reference Ag (Ag is more oxidized). This can be caused by the dilution of Pt by alloying with Ag in small NPs and the charge transfer from Ag to Pt.[44,45] Both of the effects indicate the alloying between Ag and Pt. The composition estimated from XPS quantitative analysis is given in Table 1, which is close to the nominal composition by mass measurement.

Composition Distribution of Pt/Ag NPs

To analyze the composition of the samples, the STEM-EDX mapping was carried out. Figure 9 is the STEM-EDX mapping images of the Pt50Ag50 obtained in PEG. The presence of Pt and Ag in the same position was observed for all single NPs in Figure 9, indicating the formation of Pt/Ag alloy NPs. The EDS spectrum for the map area of a single particle (Figure S8) shows the signal of Pt and Ag is low but distinguishable from the background. The elemental line profile of several single NPs (Figure S9) shows the

Pt and Ag at the same regions. However, the count number in the line profile is also low, which can be insufficient to assess the elemental ratio for some positions in the particle with high confidence. This is because the NPs are small and they moved or were damaged so we could not have a long time scan to increase the count numbers. The STEM-EDX mapping images of Pt50Ag10 and Pt10Ag50 are shown in Figures S10 and S4, respectively. Aside from Pt/Ag alloy, pure Pt NPs and some pure Ag NPs were observed in Pt50Ag10 and Pt10Ag50 samples, respectively.

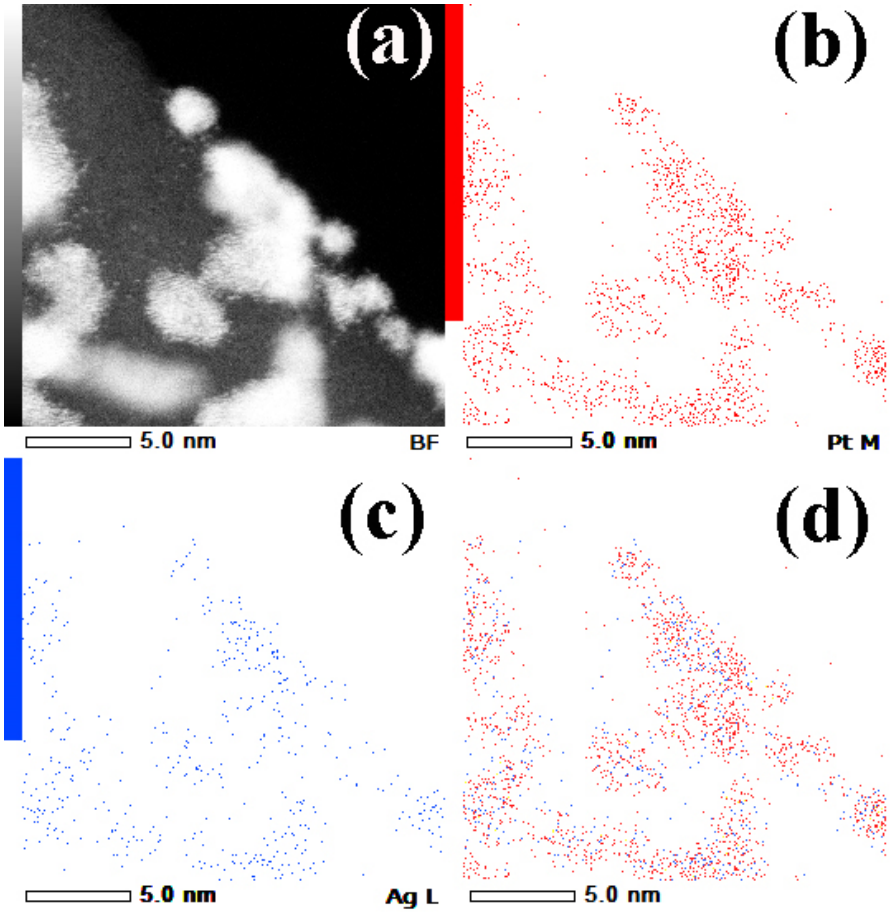

Figure 9. (a) HAADF image and (b-d) STEM-EDS mapping images of Pt50Ag50 NPs: (b) Pt M, (c) Ag L, and (d) overlapping image of Pt and Ag.

Based on EDX mapping results, the composition distributions in Pt/Ag NPs for 3 samples sputtered onto PEG and on TEM grids are plotted in Figure 10 wherein the horizontal axis is the atomic composition of Pt over the total amount of Pt and Ag and the vertical axis shows the population of the composition detected in the samples.

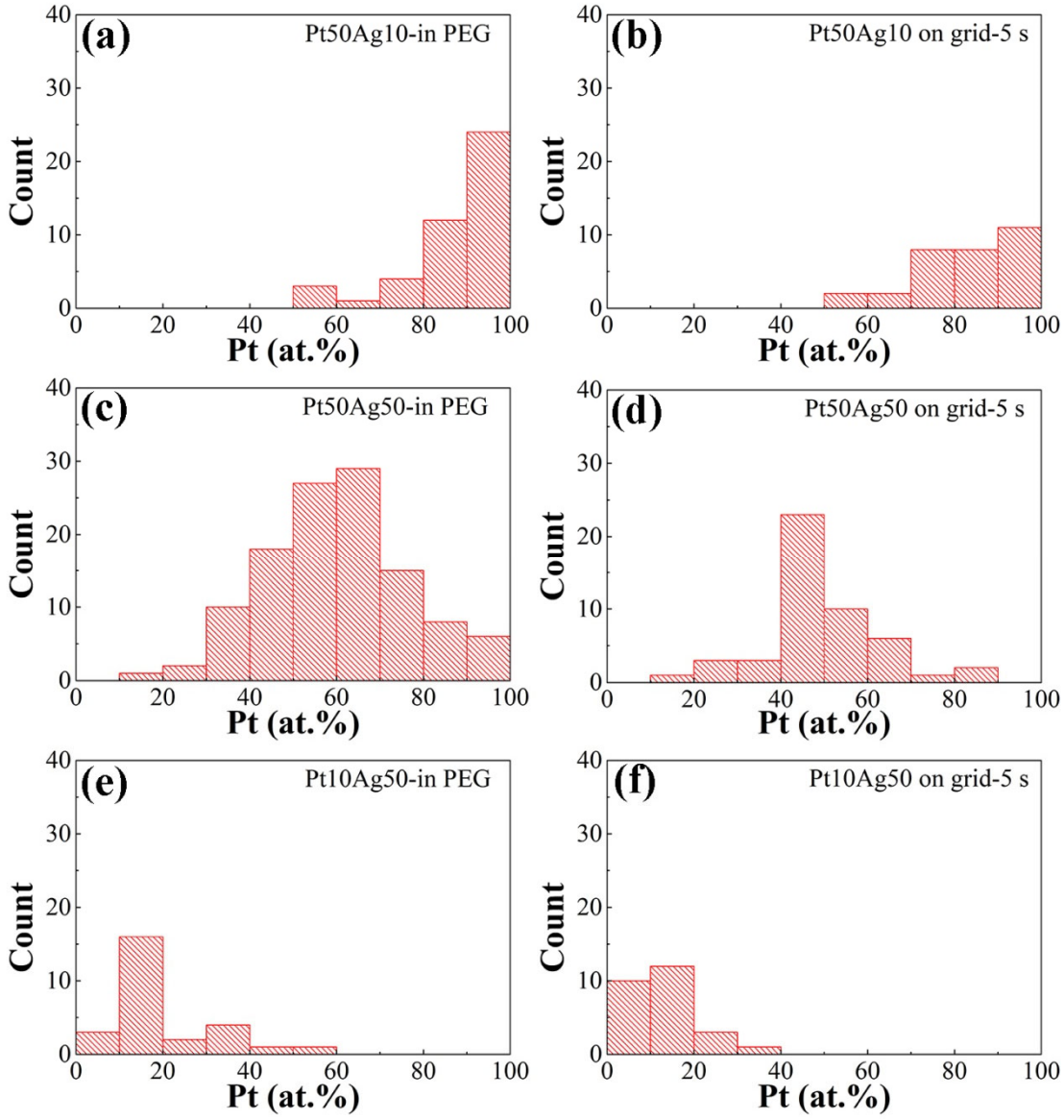

Figure 10. Composition distributions of sample Pt50Ag10, Pt50Ag50, and Pt10Ag50 sputtered onto PEG (a, c, e) and on TEM grids for 5 s (b, d, f). The numbers of the NPs measured with STEM-EDX for plotting in Figures 10a-10f are 45, 31, 117, 49, 28, and 26, respectively.

For the samples sputtered onto PEG, the result showed that Pt50Ag10 contained Pt/Ag NPs with Pt of more than 50 at. % and a large number of pure Pt NPs, Pt10Ag50 contained Pt/Ag NPs with Pt less than 60 at. % and a small number of pure Ag NPs whereas the composition of Pt in Pt50Ag50 ranged from 10 to 100 at. % in standard Gaussian distribution without pure Ag but with a small number of pure Pt NPs. The average values of Pt content in Pt50Ag10, Pt50Ag50, and Pt10Ag50 sputtered onto PEG were 85.1 ± 14.0, 60.2 ± 16.2, and 19.8 ± 12.2 at. %, respectively. This result revealed that a higher current of Pt leads to the higher content of Pt in Pt/Ag samples, which is consistent with the above XRD and HAADF results. Further, for each pair of sputtering currents, it was observed that the composition distributions of the samples sputtered onto PEG and on the TEM grid for 5 s shared a similar feature (the STEM-EDX mappings of samples with 5 s sputtering on grids are in Figures S11-S13). Thus, it was suspected that the initial combination and nucleation in the vacuum and/or nucleation/growth on the PEG surface regulated the composition distributions. In particular, compositions of Pt50Ag10 and Pt10Ag50 were primarily determined by the element with a dominant population in the sputtering chamber via homogenous nucleation and growth by the collision of atoms/clusters from the same element. As a result, pure Pt and Ag were obtained in Pt50Ag10 and Pt10Ag50, respectively. When the amounts of the ejected Pt and Ag atoms are relatively sufficient and balanced to each other, as in Pt50Ag50, the atoms/clusters from different elements could combine more effectively at a higher probability during both nucleation and growth, thus,

decreasing the amount of pure Pt and Ag and increasing Pt/Ag alloy NPs.

Table 1. Pt at % in Pt/Ag by mass measurement, EDS, and XPS analysis

Sample	Nominal Pt (at. %) by mass measurement*	Pt (at. %) by STEM-EDS†	Pt (at. %) by XPS‡	Mass of NPs (mg) *,‖
Pt50Ag10	90.9	85.1 ± 14.0	87.9	1.65
Pt50Ag50	55.9	60.2 ± 16.2	44.4 (43.5†)	2.24
Pt10Ag50	11.9	19.8 ± 12.2	8.4	0.85

*sputtered onto Al foil; †NPs sputtered onto PEG (30 min); ‡NPs sputtered on Si (10 s); ‖ estimated for 30 min sputtering

Table 1 shows the nominal composition of Pt and Ag estimated from the weight of Pt and Ag sputtered on Al foils (Table S1). The Pt nominal compositions of Pt50Ag10, Pt50Ag50, and Pt10Ag50 are 90.9, 55.9, and 11.9 at. %, respectively. Sample Pt50Ag50 sputtered in PEG had Pt content of 60.2 ± 16.2 at. %, close to the nominal composition (55.9 at. %), whereas bigger differences between the nominal and measured Pt at. % of Pt/Ag NPs in PEG were observed for samples Pt50Ag10 and Pt10Ag50. Especially, in Pt10Ag50 sputtered in PEG, agglomerates of Ag (Figure 2) further decreased the content of Ag in Pt/Ag alloy NPs and made the composition of Pt became higher than the nominal value. On the other hand, there may exist some pure and small Pt NPs and/or nanoclusters in sample Pt50Ag10 sputtered onto PEG of which the composition could not be measured accurately in STEM-EDS, leading to a lower composition of Pt in the alloy NPs compared to the nominal value.

Relation of Composition Distribution, Particle Size, and Particle Formation in Pt/Ag NPs

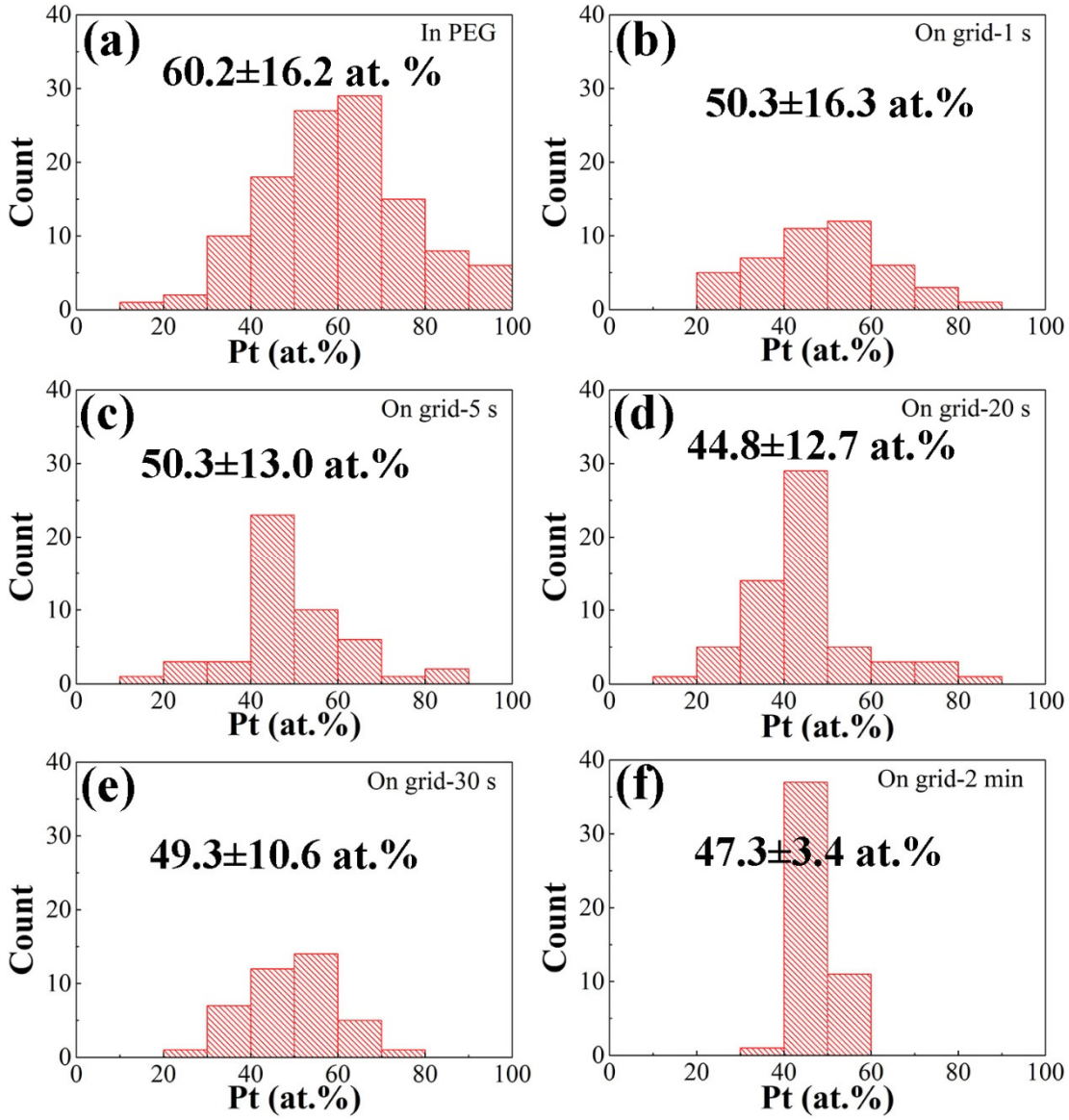

Figure 11. Composition distributions of (a) Pt50Ag50 sputtered in PEG for 30 min and Pt50Ag50 sputtered on grid for (b) 1 s, (c) 5 s, (d) 20 s, (e) 30 s and (f) 2 min.

To investigate the impact of PEG on the particle composition and growth as well as the impact of particle growth on the composition distribution, the composition and size

distribution of Pt50Ag50 NPs sputtered onto PEG were compared with that on TEM grids for different sputtering times (1 s -2 min) as shown in Figure 11. The compositions from STEM-EDS mappings (Figures S13-S17) were collected by measuring single particles or grains of about 2 nm (in the 30 s and 2 min sputtering). The composition distributions of the samples sputtered on the TEM grids became narrower along with the increase of the particle sizes for a longer sputtering time from 1.4 (1 s) to 2.6 nm (20 s) and bigger sizes with aggregation, necking (30 s), and connecting matrix (2 min sputtering) (Figure S18). This suggested that Pt atoms and Ag atoms randomly distributed and combined initially in a wide composition distribution and small particle size. On the solid substrate, these particles could not move. Thus, as sputtering time increased, the small NPs combined with more sputtered atoms. Consequently, the particle size became bigger and composition at one position (grain) became more uniform. It was observed that the sample Pt50Ag50 obtained in PEG had the composition distribution close to that obtained by sputtering on the TEM grid for 5 s and 20 s but broader than Pt50Ag50 sputtered on TEM grids for longer times (30 s, 2 min). The particle size of the sample in PEG (1.8 ± 0.3 nm, Figure S1) was somehow larger than that of Pt/Ag NPs sputtered on TEM grid for 5 s (1.6 ± 0.3 nm) and much smaller than that on the TEM grids for 20 s (2.6 ± 0.3 nm) (Figure S18) or more. This result indicated that PEG could hinder the formed NPs from combining with other atoms/clusters and growing to bigger sizes, to some extent. Hence, PEG supported the formation and growth of NPs with more uniform sizes. The effect comes from the high viscosity of PEG and its binding to NPs via the terminal –OH group and O in -CH_2-

CH_2-O- units as suggested by Hatakeyama et al.[28] The -CH_2-CH_2- units of PEG can surroundadd a steric hindrance to NPs.[28] We observed a bigger size and some agglomerations of Pt50Ag50 NPs sputtered in silicone oil (KF-96-100cs, Shin-Etsu) of similar viscosity with PEG but without –OH and -CH_2-CH_2-O- units to stabilize NPs (Figure S19). Further, the results of composition distribution and size are in good agreement with the above hypothesis that the composition distribution of this sample is regulated by the initial nucleation and growth of Pt/Ag clusters in the vacuum and/or PEG surface.

Conclusion

In this work, Pt/Ag alloy NPs were successfully synthesized by co-sputtering method and the alloy NPs were proved to be solid-solution of PtAg. The average sizes Pt/Ag samples had no obvious change with different sputtering currents in the range of 10-50 mA. However, the sputtering currents could affect the peak positions in XRD results, which was mainly caused by the distribution of the alloy composition in the samples. By comparing the composition distributions and size distributions of the samples sputtered onto PEG and on glass, it is found that PEG could hinder the NPs from growing to larger sizes as well as agglomerating. However, this also contributed to the formation of the broader size distribution of Pt/Ag NPs formed in PEG compared with NPs and thin films formed on TEM solid substrates or glass. The relationship between the sputtering currents, thereby particle compositions, and the formation of the samples, can pave the way to a better understanding of the solid solution alloy formation via

sputtering technique onto liquid polymer.

ASSOCIATED CONTENT

Supporting Information. Size distributions of Pt/Ag NPs obtained from measuring particle sizes in TEM images; Relation between particle size and sputtering currents of Pt/Ag NPs obtained in PEG; Photograph of PEG-NPs dispersions of Pt/Ag NPs obtained by sputter deposition onto PEG with various sputtering currents; XRD patterns of Pt/Ag sputtered onto the glass slices for different times; HAADF-STEM and EDX mapping of Pt/Ag NPs sputtered onto PEG; STEM-HAADF images and size distributions of Ag/Pt sputtered onto TEM grids for 1 s to 2 min; The amount of Pt and Ag on Al foil for 30 min sputtering; EDS spectra of Pt/Ag NPs. XPS spectra of Pt50Ag50 NPs; TEM image and size distribution of Pt50Ag50 sputtered onto silicone oil; The XPS peak position of Pt/Ag, Pt, and Ag NPs sputtered on Si wafer for 10 s.

The following file (PDF) is available free of charge.

AUTHOR INFORMATION

Corresponding Author

*Email: mai_nt@eng.hokudai.ac.jp, tetsu@eng.hokudai.ac.jp

Author Contributions

The manuscript was written through contributions of all authors. All authors have given approval to the final version of the manuscript.

FUNDING SOURCES

A part of this work conducted at Hokkaido University was supported by “Nanotechnology Platform” program of the Ministry of Education, Culture, Sports, Science and Technology-Japan (MEXT). MTN acknowledges partial financial support by Grant-in-Aid for Scientific Research for Young Researcher (B) from JSPS (17K14072), Young Research Eccelaration Project of Hokkaido University, Grant for Basic Science Research Projects from the Sumitomo Foundation (180584), and the Kurata Grant awarded by the Hitachi Global Foundation. TY thanks partial financial support by Grant-in-Aid for Scientific Research (B) (18H01820) and Grant-in-Aid for Scientific Research on Innovative Areas (Research in a proposed research area) (19H05162) from JSPS. Partial financial support from the Cooperative Research Program of “Network Joint Research Center for Materials and Devices.” (20201248, 20191100, and 20191253) is gratefully acknowledged. Part of this research was conducted at Laboratory of XPS analysis and at “Joint-Use Facilities: Laboratory of Nano-Micro Material Analysis”, Hokkaido University, supported by “Nanotechnology Platform” Program of the Ministry of Education, Culture, Sports, Science and Technology (MEXT), Japan.

ACKNOWLEDGEMENT

This work is partially supported by Hokkaido University. Authors thank Mr. T. Tanioka, Ms. R. Ishikawa, and Mr. R. Oota (Hokkaido University) for their assistance in TEM observation. We thank Ms. N. Hirai and Ms. Y. Mori (Hokkaido University) for fruitful discussion and assistance in STEM observation and STEM-EDX analysis.

We thanks Mr. K. Suzuki for his support in XPS measurement. M. Z. thanks the Ministry of Education, Culture, Sports, Science and Technology-Japan (MEXT) for financial support for her stay in Sapporo.

References

1. Li, Y.; Gao, W.; Ci, L.; Wang, C.; Ajayan, P. M. Catalytic performance of Pt nanoparticles on reduced graphene oxide for methanol electro-oxidation. *Carbon* **2010**, *48*, 1124-1130.
2. Mostafa, S.; Behafarid, F.; Croy, J. R.; Ono, L. K.; Li, L.; Yang, J. C.; Frenkel, A. I.; Cuenya, B. R. Shape-dependent catalytic properties of Pt nanoparticles. *J. Am. Chem. Soc.* **2010**, *132*, 15714-15719.
3. Liu, Z.; Gan, L. M.; Hong, L.; Chen, W.; Lee, J. Y. Carbon-supported Pt nanoparticles as catalysts for proton exchange membrane fuel cells. *J. Power Sources* **2005**, *139*, 73-78.
4. Xiong, B.; Zhou, Y.; Zhao, Y.; Wang, J.; Chen, X.; O'Hayre, R.; Shao, Z. The use of nitrogen-doped graphene supporting Pt nanoparticles as a catalyst for methanol electrocatalytic oxidation. *Carbon* **2013**, *52*, 181-192.
5. Mu, Y.; Liang, H.; Hu, J.; Jiang, L.; Wan, L. Controllable Pt nanoparticle deposition on carbon nanotubes as an anode catalyst for direct methanol fuel cells. *J. Phys. Chem. B* **2005**, *109*, 22212-22216.
6. Song, P.; Xu, H.; Yan, B.; Wang, J.; Gao, F.; Zhang, Y.; Shiraishi, Y.; Du, Y. Particle size effects of PtAg nanoparticles on the catalytic electrooxidation of liquid fuels.

Inorg. Chem. Front. **2018**, *5*, 1174-1179.

7. Zhou, X.; Gan, Y.; Du, J.; Tian, D.; Zhang, R.; Yang, C.; Dai, Z. A review of hollow Pt-based nanocatalysts applied in proton exchange membrane fuel cells. *J. Power Sources* **2013**, *232*, 310-322.
8. Zhang, G.; Yang, Z.; Zhang, W.; Hu, H.; Wang, C.; Huang, C.; Wang, Y. Tailoring the morphology of Pt_3Cu_1 nanocrystals supported on graphene nanoplates for ethanol oxidation. *Nanoscale* **2016**, *8*, 3075-3084.
9. Fu, G.; Xia, B.; Ma, R.; Chen, Y.; Tang, Y.; Lee, J. Trimetallic PtAgCu@PtCu core@shell concave nanooctahedrons with enhanced activity for formic acid oxidation reaction. *Nano Energy* **2015**, *12*, 824-832.
10. Zheng, L.; Yang, D.; Chang, R.; Wang, C.; Zhang, G.; Sun, S. Crack–tips enriched platinum–copper superlattice nanoflakes as highly efficient anode electrocatalysts for direct methanol fuel cells. *Nanoscale* **2017**, *9*, 8918-8924.
11. Zhang, B.; Zhang, Z.; Liao, H.; Gong, Y.; Gu, L.; Qu, X.; You, L.; Liu, S.; Huang, L.; Tian, X.; Huang, R.; Zhu, F.; Liu, T.; Jiang, Y.; Zhou, Z.; Sun, S. Tuning Pt-skin to Ni-rich surface of Pt_3Ni catalysts supported on porous carbon for enhanced oxygen reduction reaction and formic electro-oxidation. *Nano Energy* **2016**, *19*, 198-209.
12. Li, Z.; Li, Y.; He, C.; Shen, P. K. Bimetallic PtAg alloyed nanoparticles and 3-D mesoporous graphene nanosheet hybrid architectures for advanced oxygen reduction reaction electrocatalysts. *J. Mater. Chem. A* **2017**, *5*, 23158-23169.
13. Dutta, S.; Ray, C.; Sasmal, A. K.; Negishi, Y.; Pal, T. Fabrication of dog-bone

shaped Au NR_{core}–Pt/Pd_{shell} trimetallic nanoparticle-decorated reduced graphene oxide nanosheets for excellent electrocatalysis. *J. Mater. Chem. A* **2016**, *4*, 3765-3776.

14. Mahmood, A.; Xie, N.; Din, M. A. U.; Saleem, F.; Lin, H.; Wang, X. Shape controlled synthesis of porous tetrametallic PtAgBiCo nanoplates as highly active and methanol-tolerant electrocatalyst for oxygen reduction reaction. *Chem. Sci.* **2017**, *8*, 4292-4298.
15. Chen, Q.; Cao, Z.; Du, G.; Kuang, Q.; Huang, J.; Xie, Z.; Zheng, L. Excavated octahedral Pt-Co alloy nanocrystals built with ultrathin nanosheets as superior multifunctional electrocatalysts for energy conversion applications. *Nano Energy* **2017**, *39*, 582-589.
16. Karakaya, I.; Thompson, W. T. The Ag-Pt (Silver-Platinum) system. *Bull. Alloy Phase Diagrams* **1987**, *8*, 334-340.
17. Fu, T.; Fang, J.; Wang, C.; Zhao, J. Hollow porous nanoparticles with Pt skin on a Ag–Pt alloy structure as a highly active electrocatalyst for the oxygen reduction reaction. *J. Mater. Chem. A* **2016**, *4*, 8803-8811.
18. Ramirez-Caballero, G. E.; Ma, Y.; Callejas-Tovar, R. and Balbuena, P. B. Surface segregation and stability of core–shell alloy catalysts for oxygen reduction in acid medium. *Phys. Chem. Chem. Phys.* **2010**, *12*, 2209-2218.
19. Peng, Z.; You, H.; Yang, H. An electrochemical approach to PtAg alloy nanostructures rich in Pt at the surface. *Adv. Funct. Mater.* **2010**, *20*, 3734-3741.
20. Douk, A. S.; Saravani, H.; Noroozifar, M. One-pot synthesis of ultrasmall Pt-Ag

nanoparticles decorated on graphene as a high-performance catalyst toward methanol oxidation. *Int. J. Hydrogen* **2018**, *43*, 7946-7955.

21. Lam, B. T. X.; Chiku, M.; Higuchi, E.; Inoue, H. PtAg Nanoparticle Electrocatalysts for the Glycerol Oxidation Reaction in Alkaline Medium. *Adv. Nanopart.* **2016**, *5*, 167-175.
22. Yousaf, A. B.; Imran, M.; Zeb, A.; Wen, T.; Xie, X.; Jiang, Y. Single Phase PtAg Bimetallic Alloy Nanoparticles Highly Dispersed on Reduced Graphene Oxide for Electrocatalytic Application of Methanol Oxidation Reaction. *Electrochim. Acta* **2016**, *197*, 117-125.
23. Ishida, Y.; Corpuz, R. D.; Yonezawa, T. Matrix Sputtering Method: A Novel Physical Approach for Photoluminescent Noble Metal Nanoclusters. *Acc. Chem. Res.* **2017**, *50*, 2986−2995.
24. Nguyen, M. T.; Yonezawa, T. Sputtering onto a liquid: interesting physical preparation method for multi-metallic nanoparticles. *Sci. Technol. Adv. Mater.* **2018**, *19*, 883-898.
25. Ye, G.; Zhang, Q.; Feng, C.; Ge, H.; Jiao, Z. Structural and electrical properties of a metallic rough-thin-film system deposited on liquid substrates. *Phys. Rev. B* **1996**, *54*, 14754-14757.
26. Torimoto, T.; Okazaki, K.; Kiyama, T.; Hirahara, K.; Tanaka, N.; Kuwabata, S. Sputter deposition onto ionic liquids: Simple and clean synthesis of highly dispersed ultrafine metal nanoparticles. *Appl. Phys. Lett.* **2006**, *89*, 243117.
27. Torimoto, T.; Tsuda, T.; Okazaki, K.; Kuwabata, S. New Frontiers in Materials

Science Opened by Ionic Liquids. *Adv. Mater.* **2010**, *22*, 1196-1221.

28. Hatakeyama, Y.; Morita, T.; Takahashi, S.; Onishi, K.; Nishikawa, K. Synthesis of Gold Nanoparticles in Liquid Polyethylene Glycol by Sputter Deposition and Temperature Effects on their Size and Shape. *J. Phys. Chem. C* **2011**, *115*, *8*, 3279–3285.
29. Wender, H.; Gonçalves, R. V.; Feil, A. F.; Migowski, P.; Poletto, F. S.; Pohlmann, A. R.; Dupont, J.; Teixeira, S. R. Sputtering onto Liquids: From Thin Films to Nanoparticles. *J. Phys. Chem. C* **2011**, *115*, *33*, 16362–16367.
30. Hirano, M.; Enokida, K.; Okazaki, K.; Kuwabata, S.; Yoshida, H.; Torimoto, T. Composition-dependent electrocatalytic activity of AuPd alloy nanoparticles prepared via simultaneous sputter deposition into an ionic liquid. *Phys.Chem. Chem. Phys.* **2013**, *15*, 7286-7294.
31. König, D.; Richter, K.; Siegel, A.; Mudring, A.; Ludwig, A. High-Throughput Fabrication of Au–Cu Nanoparticle Libraries by Combinatorial Sputtering in Ionic Liquids. *Adv. Funct. Mater.* **2014**, *24*, 2049–2056.
32. Nguyen, M. T.; Yonezawa, T.; Wang, Y.; Tokunaga, T. Double Target Sputtering into Liquid: A New Approach for Preparation of Ag-Au Alloy Nanoparticles. *Mater. Lett.* **2016**, *171*, 75-78.
33. Nguyen, M. T.; Zhang, H.; Deng, L.; Tokunaga, T.; Yonezawa, T. Au/Cu Bimetallic Nanoparticles via Double-Target Sputtering onto a Liquid Polymer. *Langmuir* **2017**, *33*, 12389-12397.
34. Deng, L.; Nguyen, M. T.; Shi, J.; Chau, Y. R.; Tokunaga, T.; Kudo, M.; Matsumura,

S.; Hashimoto, N.; Yonezawa, T. Highly Correlated Size and Composition of Pt/Au Alloy Nanoparticles via Magnetron Sputtering onto Liquid. *Langmuir* **2020**, *36*, 3004-3015.

35. Chau, Y. R.; Nguyen, M. T.; Zhu, M.; Romier, A.; Tokunaga, T.; Yonezawa, T. Synthesis of composition-tunable Pd–Cu alloy nanoparticles by double target sputtering. *New J. Chem.* **2020**, *44*, 4704-4712.
36. Vegard, L. Die Konstitution der Mischkristalle und die Raumfüllung der Atome. *Z. Phys.* **1921**, *5*, 17-26.
37. H. Okamoto. Ag-Pt (silver-platinum), *J. Phase Equilibria*, **1997**, *18* (5), 485.
38. G. L. W. Hart, L. J. Nelson, R. R. Valfleet, B. J. Campbell, M. H. F. Sluiter, J. H. Neethling, E. J. Olivier, S. Allies, C. I. Lang, B. Meredig, C. Wolverton. Revisiting the revised Ag-Pt phase diagram. *Acta Mater.* 2017, **124**, 325-332.
39. http://materialsproject.org (A. Jain*, S.P. Ong*, G. Hautier, W. Chen, W.D. Richards, S. Dacek, S. Cholia, D. Gunter, D. Skinner, G. Ceder, K.A. Persson *(*=equal contributions). The Materials Project: A materials genome approach to accelerating materials innovation.* APL Materials, 2013, 1(1), 011002.)
40. J. Pirat, A. Font, D. Rapetti, C. Andreazza-Vignolle, P. Andreazza, C. Mottet, R. Ferrando. Reversed size-dependent stabilization of ordered nanophases. *Nat. Commun.*, **2019**, *10*, 1982.
41. S. Suzuki, Y. Tomita, S. Kuwabata, T. Toromoto. Synthesis of alloy AuCu nanoparticles with the $L1_0$ structure in an ionic liquid using sputter deposition. *Dalton Trans.*, **2015**, *44*, 4186-4194.

42. Z. Peng, H. Yang. Ag-Pt alloy nanoparticles with the compositions in the miscibility gap. *J. Solid State Chem.*, **2008**, *181*, 1546-1551.

43. Handbook of X-ray Photoelectron Spectroscopy, JEOL 1991, Ed. by N. Ikeo, Y. Iijima, N. Nishimura, M. Sigematsu, T. Tazawa, S. Matsumoto, K. Kojima, Y. Nagasawa.

44. T. Diemant, K. M. Schüttler, R. J. Behm. Ag on Pt(111): Changes in Electronic and CO Adsorption Properties upon PtAg/Pt(111) Monolayer Surface Alloy Formation. *ChemPhysChem*, **2015**, *16*, 2943 – 2952.

45. N. Sui, K. Wang, X. Shan, Q. Bai, L. Wang, H. Xiao, M. Liu, V. L. Colvin, W. W. Yu. Facile synthesis of hollow dendritic Ag/Pt alloy nanoparticles for enhanced methanol oxidation efficiency. *Dalton Trans.*, **2017**, *46*, 15541–15548.

For Table of Contents Only